Journal of Materials Chemistry C

Accepted Manuscript

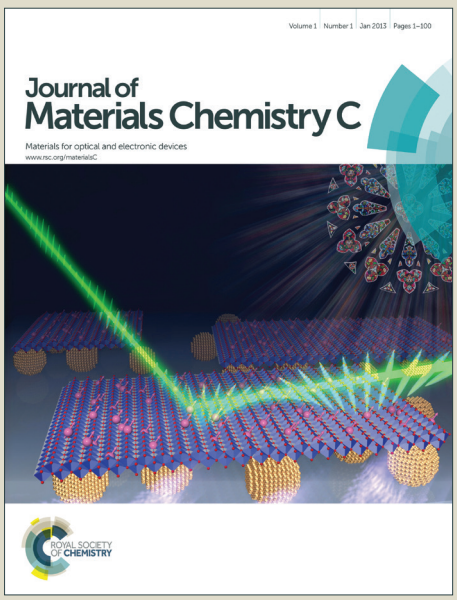

ROYAL SOCIETY OF CHEMISTRY

www.rsc.org/materialsC

Effect of oxygen vacancy on the structural and electronic characteristics in crystalline Zn_2SnO_4

Joohwi Lee[a,b,c], Youngho Kang[b], Cheol Seong Hwang[b,c], Seungwu Han[b], Seung-Cheol Lee[a], and Jung-Hae Choi[a,*]

[a] Electronic Materials Research Center, Korea Institute of Science and Technology, Seoul 136-791, Korea

[b] Department of Materials Science and Engineering, Seoul National University, Seoul 151-744, Korea

[c] Inter-university Semiconductor Research Center, Seoul National University, Seoul 151-744, Korea

[*]Corresponding author. Tel.: +82 2 958 5488; Fax: +82 2 958 6658.

E-mail address: choijh@kist.re.kr (J.-H. Choi).

Abstract

The effects of oxygen vacancies on the atomic and electronic structures in crystalline Zn_2SnO_4 were examined by *ab-initio* calculations using screened hybrid density functional. The formation energy and the electronic structure indicated that the neutral oxygen vacancy was stable in the n-type region with forming deep level in the bandgap. The ionization energy of oxygen vacancy was calculated to be around 2.0 eV, which can be excited by visible photon energy. The atomic movements and the Bader charge analyses around the neutral oxygen vacancy showed that Sn played a dominant role in changing the electronic properties by forming the pair of Sn^{2+}-V_O^0, which was accompanied by the reduction of the charge state of Sn due to its multiple oxidation states. On the contrary, the electronic state of Zn hardly changed despite of its more predominant atomic shifts than Sn around the oxygen vacancy.

Keywords;

Ab-initio calculations, inverse spinel Zn_2SnO_4, oxygen vacancy, atomic structure, electronic structure

1. Introduction

Due to the high mobility and optical transparency, the transparent oxide semiconductors (TOSs) with the wide bandgap (> ~3 eV) have been studied for optoelectronic devices, such as displays and solar cells.[1,2] Among them, zinc tin oxide (ZTO; Zn_2SnO_4), is one of the most promising materials due to its non-toxicity and low cost as well as the good optical and electrical properties compared to the indium gallium zinc oxides (InGaZnO).[3-5] Similar to the other Zn-based oxides, the concentration of the n-type charge carrier in ZTO has been reported to be $10^{18} \sim 10^{19}/cm^3$ in its unintentionally doped state.[6]

The thermodynamic stability and role of oxygen vacancies have been equivocal according to the formation condition and the kind of the elements for various n-type conducting oxides.[7-14] According to the theoretical reports, the neutral oxygen vacancy (V_O^0) exists with the formation of the deep level in the bandgap for the binary oxides such as ZnO and SnO_2.[7-10] For multi-component oxides such as InGaZnO, the V_O was also reported to form the deep level with neutral charge state.[11,12] For this reason, the deep state in the bandgap generated by V_O was believed to be one of the factors which resulted in the problems related with the negative bias illumination stability in devices.[13] In contrast, the doubly charged oxygen vacancy (V_O^{2+}) is thermodynamically stable in different n-type oxides such as TiO_2.[14]

To the authors' knowledge, however, the theoretical calculations on the defects in ZTO have been rarely performed. As the forefront work for the ternary oxides, this work

reports the role of the oxygen vacancy on the atomic and electronic structures in zinc tin oxide. In multi-component oxide systems, the effects of the changes in the charges of cations have been of interest.[15] Zn has multiple preference on the site occupancy for forming bonds with O, which induced the diverse coordination numbers (CNs) of Zn and the bond lengths of Zn-O in various crystalline phases[16] as well as the amorphous phase.[17] On the other hand, the CNs of Sn and bond lengths of Sn-O are almost constant in various oxide materials containing Sn. Meanwhile, it should be pointed out that the majority carrier types are opposite in SnO (hole) and SnO_2 (electron), which could be changed from one type to the other according to the Sn and O ratio.[18-20] Low oxidation numbers of Sn were also found in O-deficient binary phases such as Sn_2O_3 and Sn_3O_4.[21]

In this paper, the changes in the atomic and electronic structures induced by the presence of an oxygen vacancy in crystalline ZTO were studied by the *ab-initio* calculations using screened hybrid functional and compared with those in its constituent binary oxides of ZnO, SnO, and SnO_2. The spatial distribution of the $|\Psi|^2$ of the localized state induced by the oxygen vacancy and the quantitative changes of charge on cations around the oxygen vacancy were also examined.

2. Computational methods

Ab-initio calculations were performed using a pseudopotential plane-wave code, the Vienna *Ab-initio* Simulation Package (VASP).[22,23] The projector augmented wave (PAW) method within the generalized gradient approximation (GGA) parameterized by Perdew et

al.(PBE),[24] PBE+U,[25] HSE06[26] and optimized HSE06 (opt-HSE06) were tested, with a cutoff energy of 500 eV. The main calculations were performed using the opt-HSE06, which showed the adjusted bandgap to the experimental value[27,28] of 3.6 eV. The 3d and 4s orbitals for Zn, 4d, 5s and 5p orbitals for Sn and 2s and 2p orbitals for O were treated as the valence electrons. One of the ordered inverse spinel structures ZTO belonging to the space group $P4_122$ was selected as a model system of the zinc tin oxide. Note that it was reported to be energetically the most stable spinel phase and its primitive cell consists of 28 atoms.[16,31] The lattice parameters of the primitive cell, a=c and b were determined to be 6.156 and 8.615 Å, respectively. One oxygen vacancy was generated in the 2×1×2 supercell composed of 112 atoms and the 2×2×2 Γ-centered k-points meshes were used for the supercell. The calculations with the oddly charged vacancy were performed with spin-polarized method.

The formation energy of an oxygen vacancy was calculated by equation (1),

$$E^f(V_O) = E_{tot}(Zn_2SnO_4 + V_O) - E_{tot}(Zn_2SnO_4) + \mu_O + q(E_F + E_{VBM}) + \Delta E_{corr} \qquad (1)$$

where, $E_{tot}(Zn_2SnO_4 + V_O)$ is the total energy of supercell with one V_O, $E_{tot}(Zn_2SnO_4)$ is the total energy of the perfect Zn_2SnO_4 supercell, μ_O is the chemical potential of an oxygen atom, E_F is the Fermi level with respect to the valence band maximum (VBM), E_{VBM} is the Kohn-Sham level of the VBM, and ΔE_{corr} is the correction for the charged V_O from the Coulombic interactions between the supercells. The static dielectric constant was calculated to be 10.0 ε_0 from the density functional perturbation theory,[32] where ε_0 is vacuum permittivity. The formation energy of the charged oxygen vacancy needs to be corrected due to the image charge interactions which depend on the size and shape of the supercells. Due to the excessive time consumption for the calculations using hybrid density functional, the correction term of image charge interaction, ΔE_{corr}, in the equation (1) was tested using

PBE+U on the supercells with 56, 112, 224 and 448 atoms. The O-rich condition was used, therefore μ_O was set as the half of the energy of O_2 molecule and the spin-polarized method were adopted for the oddly charged vacancy.

In order to determine the quantitative charge transfer around the V_O, a grid-based Bader analysis was carried out with the correction of core charge.[33,34] In addition, the $|\Psi|^2$ plots for the state generated by the V_O were also obtained. Visualizations for atomic structures and $|\Psi|^2$ plots were obtained by VESTA program.[35]

The binary oxides, ZnO and SnO_2 were also examined for comparison. The opt-HSE06 was also used, with the fraction of the exact exchange energy of 37.5 % for ZnO and 32 % for SnO_2 to adjust their experimental bandgap values, respectively. [36]

3. Results and discussions

3.1. Formation energy

Table 1 shows the calculated bandgaps obtained by using PBE, PBE+U, HSE06 and opt-HSE06 in comparison with the experimental value. For the opt-HSE06, the fraction of the exact exchange energy was 29 % and all values are the direct bandgaps.

Fig. 1a is the atomic structure for the supercell of the perfect ZTO showing that the Sn and Zn atoms are arranged in the ordered manner. Fig. 1b shows two oxygen sites in ZTO.

The *O-A site* is surrounded by 3 Zn and 1 Sn atoms, while *O-B site* surrounded by 2 Zn and 2 Sn atoms, respectively and the number of each site is identical. The cation sites are categorized by the one tetrahedral site, *tet-I site* and three octahedral sites, *oct-I*, *oct-II* and *oct-III*. The tetrahedral site is always occupied by Zn. In contrast, the octahedral sites are occupied by 1 Sn and 2 Zn atoms for the *O-A site*, while they are occupied by 2 Sn and 1 Zn atoms for the *O-B site*, respectively. From now on, the oxygen vacancy formed at *O-A* and *O-B* sites will be referred to as the *O-A vacancy* and *O-B vacancy*, respectively.

Fig.2a and Fig.2b show the formation energies of the singly (V_O^+) and doubly charged oxygen vacancies (V_O^{2+}) at the *O-A site* according to the various correction methods as a function of 1/L using PBE+U, where L is the supercell size. Each curve corresponds to the non-corrected (NC) case, potential aligned (PA) case, the first term of Makov-Payne (MP),[37,38] MP with potential aligning (MPPA), and Lany-Zunger (LZ) correction.[39,40] The PA is the alignment of electrostatic potentials between the farthest region in the supercell containing a defect and a pure supercell. After the correction on each supercell, the formation energies were fitted as a function of $L^{-1} + L^{-3}$. The zero value in the x-axis means the infinitely large supercell.

The variations in the formation energy for V_O^+ and V_O^{2+} by the various methods in the infinitely large supercell were in the range of 0.06 eV. For V_O^+, the differences between the converged value and fitted values were similar as shown in Fig. 2a. For V_O^{2+}, however, the fitted value after the LZ correction was the closest to the converged value for the infinite L as shown in Fig. 2b. In addition, the differences between values at the infinite distance and

those from small supercells are the smallest. The LZ correction showed the best description, hence, was applied to main calculations using the hybrid density functional.

Fig. 3 shows the formation energy of the V_O as a function of the E_F using the opt-HSE06 with the LZ correction.[39,40] The formation energy of the *O-A vacancy* was slightly lower than that of the *O-B vacancy* in the whole E_F range. When the Fermi level is near the conduction band minimum (CBM), the neutral V_O^0 is stable. The V_O in ZTO also show the negative U behavior as in ZnO and SnO_2;[7,10] the stable charge state is directly shifted from the doubly charged state to the neutral state with the transition levels ε(+2/0) at 0.93 and 0.96 eV from the CBM for the *O-A* and *O-B vacancies*, respectively. Considering that ZTO is an n-type semiconductor,[6] the fact that V_O exists as a neutral state implied that the V_O does not play a role as the source of electrons. When the Fermi level is near the VBM, however, the V_O^{2+} is stable and its formation energy is negative, implying the oxygen vacancy can act as the killer of p-type dopant.[41] If the O-poor condition is considered, the doping probability of p-type dopant becomes more difficult because the formation energy of the V_O^{2+} becomes more negative.[42]

3.2. Atomic and electronic structures

The relaxed atomic positions of the first-nearest-neighbor cations around the V_O were summarized in Table 2 according to the charge state of the V_O in comparison with the perfect ZTO. The position of the V_O was assumed to be the same as that of O in the perfect ZTO. For the perfect ZTO, the distance of Zn-O for the *tet-I* is the shortest. Among the octahedral sites, the Sn-O distance is shorter than Zn-O distances. The atomic position shifts

of the second- and further-nearest-neighbors are negligible compared to those of the first-nearest-neighbor cations.

When the V_O^0 formed, Zn and Sn moved to the opposite directions; The Sn atom at the *oct-I site* moved towards the V_O^0 with distances reduced by 15% and 10% for the *O-A* and *O-B vacancies*, respectively. Another Sn atom at the *oct-III site* next to the *O-B vacancy* moved inward with 3% shortened distance. This means that the Sn atoms have a tendency to accommodate the localized electrons around V_O^0. The behavior of Sn atoms in ZTO is comparable to the 8~10 % shortening of the Sn-V_O^0 distance in SnO_2. In contrast, Zn atoms in the octahedral sites and those in the tetrahedral sites moved outwards with about 4~6 % and 10 % elongation of the bond lengths, respectively, presumably due to the concentrating Sn atoms around V_O. The behavior of Zn atoms in ZTO is different from the 3~4 % inward movement of Zn atoms toward V_O^0 in ZnO in this study and previous report using LDA+U method.[8]

As the charge state of the V_O became higher, the distances of Sn-V_O and Zn-V_O gradually increased for all the cations and V_O sites. The Sn-V_O distances for the V_O^+ were comparable to the Sn-O distance in the perfect ZTO. When the V_O^{2+} formed, all the atoms moved outwards from the V_O site with 8~12 % of elongation in bond lengths, due to the repulsion between the cations and positively charged V_O. The tetrahedral Zn atoms move further than octahedral atoms with 29~32 % elongation in bond length.

In order to understand the change of electronic structure generated by the V_O, the band structure diagrams and the projected density-of-states (PDOSs) of cations in ZTO with

and without V_O are presented in Fig. 4. The *O-A vacancy* was selected for showing the electronic structures with an oxygen vacancy. The occupied and unoccupied bands are demonstrated as solid and dashed lines, respectively. The electronic structure for a perfect ZTO in Fig. 4a shows a direct bandgap of 3.6 eV at Γ-point. Note that the CBM is delocalized showing a large curvature which reflects a good n-type conductivity of this material.

When the V_O^0 is formed, a very deep state occurred in the midgap region for both atomic configurations with and without atomic relaxation in Fig. 4b and Fig. 4c, respectively. This suggests that the V_O^0 formed the deep localized levels with the occupation of two electrons. Fig. 4f shows the PDOSs of the Sn at *oct-I* and Zn at *oct-II* sites, which are located at the two nearest octahedral sites from the V_O^0. Even before the atomic relaxation, the peak height of Sn is higher than that of Zn. After the atomic relaxation, the peak height of Zn reduced and that of Sn became relatively broader by the outward movement of Zn and inward movement of Sn. This also suggests that the deep localized level formed by V_O^0 is confined on Sn. PDOSs for the perfect ZTO are also shown for comparison. For the V_O^{2+}, on the other hand, the atomic relaxation showed a crucial effect on the band structure: Before the relaxation in Fig. 4d, an unoccupied deep level was found. After relaxation in Fig. 4e, however, the defect level shifted up and was located above the CBM.

The Kohn-Sham levels generated by V_O of various charge states are arranged in Table 3 for the *O-A* and *O-B vacancies*. The location of each level was estimated from the comparison of the PDOSs of cations adjacent to V_O for both the unrelaxed and relaxed atomic configurations.[14] When the singly charged vacancy (V_O^+) formed, the band which are

able to occupy two electrons were splitted into the up-spin and down-spin states and only the up-spin state is occupied by one electron. The averaged location of generated by V_O^+ after the atomic relaxation was between those of V_O^0 and V_O^{2+}.

Fig. 5a and Fig. 5b show the $|\Psi|^2$ plots of the localized band occupied by two electrons induced by the V_O^0 for the *O-A vacancy* and *O-B vacancy,* respectively. The viewing directions are identical to Fig. 1b, and Fig. 5a corresponds to the midgap state in Fig. 4c. For both *O-A vacancy* and *O-B vacancy*, the isosurface was confined around the V_O. Note that the isosurface touches Sn atom and oxygen atoms which are adjacent to the cations with the shape of p orbitals. In contrast, the isosurface does not touch the Zn atoms, indicating the localized states are strongly confined to Sn atoms.

Fig. 6a and Fig. 6b show the schematic atomic configuration diagrams to investigate the optical ionization energies for the *O-A* and *O-B vacancies* when the E_F is located at the CBM. Formation energies of V_O^0, V_O^+ and V_O^{2+} were calculated for intermediate atomic configurations as well as the stable configurations. The movement of Sn at the *oct-I site* was selected as the representative value for the atomic configurations.

The optical ionization energy from V_O^0 to ($V_O^+ + e^-$) and that from ($V_O^+ + e^-$) to ($V_O^{2+} + 2e^-$) were calculated to be 1.97 eV and 1.91 eV for the *O-A vacancy*, while they were 1.83 eV and 1.83 eV for the *O-B* vacancy, respectively. For ZnO, the measured ionization energy was reported to be ~ 2.0 eV by optical detection of electron paramagnetic resonance.[43] For the crystalline ZTO, however, the ionization energy has not been measured to the authors' knowledge. Instead, Görrn *et al*. reported that the thin film transistor composed of the

amorphous ZTO channel was remained as the off-state by the red light illumination with the energy of 1.95 eV, but became the on-state by the green light illumination with energy of 2.30 eV.[44] Despite some discrepancy in the quantitative value presumably due to the amorphous state and the correction of formation energy, the V_O^0 state located at 1.8 ~ 2.0 eV above VBM is suggested to play a role as one of the photocurrent sources by visible light photon energy.

3.3. Bader charge analysis

Table 4 shows the grid-based Bader analyses of the four first-nearest-cations around the V_O for the *O-A* and *O-B vacancies*. The Bader charges of Zn^{2+}, Sn^{2+} and Sn^{4+} obtained from the binary oxides of ZnO, SnO and SnO_2, which were obtained as the references, were 1.33, 1.35 and 2.64, respectively. The Bader charges of tetrahedral Zn, octahedral Zn and octahedral Sn in the perfect ZTO were calculated to be 1.37, 1.36 and 2.52, respectively, which are comparable to those in their binary oxides. The Bader charges of O atoms at the *O-A* and *O-B* sites in perfect ZTO were -1.33, -1.30, respectively.

For the *O-A vacancy*, the Bader charge of Sn at the *oct-I* site decreased to 1.93 and further decreased to 1.64 by the atomic relaxation next to V_O^0. Note that this value is close to the Bader charge of Sn in SnO, indicating the occupied electrons were located at Sn atom when V_O^0 formed. When the V_O^{2+} is considered, the Bader charge of Sn next to the V_O almost recovered the value in perfect ZTO by the atomic relaxation. The occupied electrons at the V_O^0 state are extracted from Sn atom when the V_O^{2+} forms. Meanwhile, the Bader charges of Zn almost unchanged by the introduction of V_O^0 and even by the V_O^{2+} irrespective

of the cation site and atomic relaxation. This is quite contrary to the significant outward movement of Zn during atomic relaxation around the charged V_O as summarized in Table 2.

For the *O-B vacancy*, two adjacent Sn atoms show the similar tendency with the one Sn atom for the *O-A vacancy*. The tendency of the change in Bader charge of Sn at the *oct-III site* was similar to that for the Sn atom at the *oct-I site*, although the degree of the change was smaller, which is consistent with the longer distance of the *oct-III site* from the oxygen vacancy as in Table 2. This implied more strongly localized charge on the Sn atom at the *oct-I* site than at the *oct-III site*. For the V_O^{2+}, the Bader charges of Sn at both the *oct-I site* and the *oct-III* site were almost the same. In contrast, the Bader charges of Zn at both the *oct-II site* and the *tet-I site* almost unchanged irrespective of the charge state of the oxygen vacancy as for the *O-A vacancy*. The Bader charges of V_O^0 of binary oxides of ZnO and SnO_2 were also examined. The Bader charge of Zn next to V_O^0 after the atomic relaxation was 1.00 in ZnO, while the values for three Sn atom2 in SnO_2 were 2.12, 2.15 and 2.28, respectively.

The strong localization of occupied electrons at one Sn atom around V_O^0 was confirmed by the atomic position shift, electronic structure, and the Bader charge and was attributed to the multi oxidation states of Sn. The nominal oxidation states of Sn can be Sn^{4+} and Sn^{2+} as in the SnO_2 and SnO, respectively, and the properties of intrinsic defects were believed to be related with the reduction of Sn^{4+} to Sn^{2+} in the SnO_2.[45] The V_O^0 with two occupied electrons reduces the Sn^{4+} to Sn^{2+}. The reduction of Sn induced by V_O was also reported in other multi-component materials such as Cu_2ZnSnS_4.[46] Ogo *et al*. reported the deep states were induced by the doping of Sn into GaZnO.[47] The previous results inferred that the pair of Sn^{2+}-V_O^0 generates the deep state in the bandgap in TCOs. In ZTO, Sn plays a

more dominant role than Zn in the changes of the electronic properties induced by the oxygen vacancy. On the other hand, the atomic relaxations around the charged oxygen vacancy are dominated by the shift of Zn position, which is analogous to its major role in the structural changes during the phase transition between various crystalline phases and amorphous phase.[16,17] Additionally, for other ordered inverse spinel Zn_2SnO_4 structures such as Imma and P1, the pair of Sn^{2+}-V_O^0 was also confirmed by the deep location of the transition level of ε(+2/0) of the oxygen vacancy as well as the inward shift and the changes in the Bader charge of Sn. This is consistent with the similar tendency for the *O-A vacancy* and the *O-B vacancy* having different configuration of the first nearest neighbors.

4. Summary

The atomic and electronic structures induced by an oxygen vacancy in crystalline ZTO were examined by the *ab-initio* calculations. The V_O^0 state with confined electrons was found to be stable in the n-type region. The ionization energy in crystalline ZTO was estimated to be around 2.0 eV, which is comparable to the previous experimental values obtained in amorphous ZTO. When the V_O^0 formed, Sn atoms shifted inward to the V_O site, while Zn atoms shifted outward from the V_O site. In addition, the Bader charge of only Sn decreased, while that of Zn hardly changed. The pair of Sn^{2+}-V_O^0 generated the deep state in the bandgap in ZTO. In the multi-component oxide of ZTO, the charge distribution and resulting electronic properties were changed mainly by Sn around the oxygen vacancy, while the electronic properties of Zn were less affected despite its atomic shift. These different

behaviors of two cations can be explained by the multiple oxidation states of Sn as well as the multiple preference on the site occupancy and diverse coordination numbers (CNs) of Zn.[16,17]

ACKNOWLEDGEMENTS

This work was supported by the IT R&D program of MOTIE/KEIT [10035320, Development of novel 3D stacked devices and core materials for the next generation flash memory], and the Institutional Research Program of KIST (2E24881). The authors would also like to acknowledge the support from the KISTI supercomputing center through the strategic support program for supercomputing application research (KSC-2013-C2-034).

REFERENCES

1 K. Nomura, H. Ohta, A. Takagi, T. Kamiya, M. Hirano, P. Hosono. *Nature*, 2004, **432**, 488.

2 P. F. Carcia, R. S. McLean, M. H. Reilly. *Appl. Phys. Lett*., 2006, **88**, 12350.

3 P. Görrn, M. Sander, J. Meyer, M. Kröger, E. Becker, H. –H. Johannes, W. Kowalsky, T. Riedl. *Adv. Mater*., 2006, **18**, 738.

4 B. S. Yang, S. Park, S. Oh, Y. J. Kim, J. K. Jeong, C. S. Hwang, H. J. Kim. *J. Mater. Chem*., 2012, **22**, 10994.

5 Y. S. Lee, J. Heo, S. C. Siah, J. P. Mailoa, R. E. Brandt, S. B. Kim, R. G. Gordon, T. Buonassisi. *Energy Environ. Sci*., 2013, **6**, 2112.

6 D. L. Young, D. L. Williamson, T. J. Coutts. *J. Appl. Phys*., 2001, **91**, 1464.

7 F. Oba, A. Togo, I. Tanaka, J. Paier, G. Kresse. *Phys. Rev. B* 2008, **77**, 245202.

8 A. Janotti, C. G. Van de Walle. *Appl. Phys. Lett*. 2005, **87**, 122102.

9 S. Lany, A. Zunger. *Phys. Rev. B*, 2010, **81**, 113201.

10 P. Ágoston, K. Albe, R. M. Nieminen, M. J. Puska. *Phys. Rev. Lett*., 2009, **103**, 245501.

11 H. Omura, H. Kumomi, K. Nomura, T. Kamiya, M. Hirano, H. Hosono. *J. Appl. Phys*., 2009, **105**, 093712.

12 A. Murat, A. U. Adler, T. O. Mason, J. E. Medvedeva. *J. Am. Chem. Soc*., 2013, **135**, 5685.

13 B. Ryu, H. -K. Noh, E. –A. Choi, K. J. Chang. *Appl. Phys. Lett*., 2010, **97**, 022108.

14 A. Janotti, J. B. Varley, P. Rinke, N. Umezawa, G. Kresse, C. G. Van de Walle. *Phys. Rev. B*, 2010, **81**, 085212.

15 U. K. Kim, S. H. Rha, J. H. Kim, Y. J. Chung, J. Jung, E. S. Hwang, J. Lee, T. J. Park, J. –H. Choi, C. S. Hwang. *J. Mater. Chem. C*, 2013, **1**, 6695.

16 J. Lee, S. –C. Lee, C. S. Hwang, J. –H. Choi. *J. Mater. Chem. C*, 2013, **1**, 6364.

17 J. Lee, Y. Kang, S. Han, C. S. Hwang, J. –H. Choi. *Appl. Phys. Lett*., 2013, **103**, 252102.

18 Y. Ogo, H. Hiramatsu, K. Nomura, H. Yanagi, T. Kamiya, M. Hirano, H. Hosono. *Appl. Phys. Lett*., 2008, **93**, 032113.

19 A. Walsh, G. W. Watson, *J. Phys. Chem. B*, 2005, **109**, 18868.

20 A. Togo, F. Oba, I. Tanaka, K. Tatsumi, *Phys. Rev. B*, 2006, **74**, 195128.

21 A. Seko, A. Togo, F. Oba, I. Tanaka. *Phys. Rev. Lett*., 2008, **100**, 045702.

22 G. Kresse, J. Furthmüller. *Phys. Rev. B*, 1996, **54**, 11169.

23 G. Kresse, J. Furthmüller. *Comput. Mater. Sci*., 1996, **6**, 15.

24 J. P. Perdew, K. Burke, M. Ernzerhof. *Phys. Rev. Lett*., 1996, **77**, 3865.

25 S. L. Dudarev, G. A. Botton, S. Y. Savrasov, C. J. Humphreys, A. P. Sutton. *Phys. Rev. B*, 1998, **57**, 1505.

26 J. Heyd, G. E. Scuseria, M. Ernzerhof. *J. Chem. Phys*., 2003, **118**, 8207. *erratum*. 2006, **124**, 219906.

27 T. J. Coutts, D. L. Young, X. Li, W. P. Mulligan, W. Wu. *J. Vac. Sci. Tech. A*, 2000, **18**, 2646.

28 B. Tan, E. Toman, Y. Li, Y. Wu. *J. Am. Chem. Soc*., 2007, **129**, 4162.

29 F. Oba, M. Choi, A. Togo, A. Seko, I. Tanaka. *J. Phys. Condens. Matter*, 2010, **22**, 384211.

30 A. K. Singh, A. Janotti, M. Scheffler, C. G. Van de walle. *Phys. Rev. Lett*., 2008, **101**, 055502.

31 A. Seko, F. Oba, I. Tanaka. *Phys. Rev. B*, 2010, **81**, 054114.

32 S. Baroni, P. Giannozzi, A. Testa. *Phys. Rev. Lett*., 1987, **58**, 1861.

33 G. Henkelman, A. Arnaldsson, H. Jónsson. *Comput. Mater. Sci*., 2006, **36**, 354.

34 W. Tang, E. Sanville, G. Henkelman. *J. Phys.: Condens. Matter*, 2009, **21**, 084204.

35 K. Momma, F. Izumi. *J. Appl. Cryst*., 2011, **44**, 1272.

36 S. Park, B. Lee, S. H. Jeon, S. Han. *Curr. Appl. Phys*., 2011, **11**, S337.

37 A. Leslie, M. J. Gillan. *J. Phys. C: Solid State Phys*., 1985, **18**, 973.

38 G. Makov, M. C. Payne. *Phys. Rev. B*, 1995, **51**, 4014.

39 S. Lany, A. Zunger. *Phys. Rev. B*, 2008, **78**, 235104.

40 S. Lany, A. Zunger. *Modelling Simul. Mater. Sci. Eng*., 2009, **17**, 084002.

41 J. Robertson, S. J. Clark. *Phys. Rev. B*, 2011, **83**, 075205.

42 A. Zunger. *Appl. Phys. Lett*., 2003, **83**, 57.

43 L. S. Vlasenko, G. D. Watkins. *Phys. Rev. B*, 2005, **71**, 125210.

44 P. Görrn, M. Lehnhardt, T. Riedl, W. Kowalsky. *Appl. Phys. Lett*., 2007, **91**, 193504.

45 K. G. Godinho, A. Walsh, G. W. Watson. *J. Phys. Chem. C*, 2009, **113**, 439.

46 K. Biswas, S. Lany, A. Zunger. *Appl. Phys. Lett*., 2010, **96**, 201902.

47 Y. Ogo, K. Nomura, H. Yanagi, T. Kamiya, M. Hirano, H. Hosono. *Phys. Stat. Sol. A*, 2008, **205**, 1920.

Table 1 Calculated bandgaps of ZTO by using various exchange-correlation functionals in comparison with the experimental value.

	Bandgap (eV)
Experimental[27,28]	3.60
PBE[24]	1.37
PBE+U[25] (Zn for 7.5 eV, Sn for 3.5 eV)[29,30]	2.20
HSE06[26]	3.33
Opt-HSE06 (fraction of exact exchange; 29 %)	3.60

Table 2 Atomic distances between V_O site and the nearest cations according to the charge state of V_O.

Site	Atomic distance (Å)					Atomic distance (Å)				
	O-A vacancy					*O-B vacancy*				
	Cation	Perfect	V_O^0	V_O^+	V_O^{2+}	Cation	Perfect	V_O^0	V_O^+	V_O^{2+}
Oct-I	Sn	2.027	1.728	1.997	2.284	Sn	2.074	1.871	2.086	2.295
Oct-II	Zn	2.056	2.146	2.223	2.294	Zn	2.213	2.327	2.337	2.386
Oct-III	Zn	2.124	2.244	2.281	2.351	Sn	2.104	2.058	2.197	2.328
Tet-I	Zn	1.982	1.999	2.440	2.627	Zn	2.031	2.235	2.473	2.631

Table 3 Locations of Kohn-Sham levels generated by V_O over VBM in eV unit.

	O-A vacancy		*O-B vacancy*	
	Unrelaxed	Relaxed	Unrelaxed	Relaxed
V_O^0	2.34	1.68	2.27	1.82
V_O^+ (up-spin)	1.05	1.98	0.98	1.97
V_O^+ (down-spin)	2.38	4.08	2.49	4.10
V_O^{2+}	1.32	5.24	1.24	5.43

Table 4 Bader charges of cations around V_O in comparison with those in perfect ZTO.

Site		Cation	Bader charges			
			Perfect	V_O^0	V_O^+	V_O^{2+}
O-A vacancy	*Oct-I*	Sn	2.52	1.64 (1.93)[a]	1.99 (2.07)	2.44 (2.26)
	Oct-II	Zn	1.36	1.30 (1.22)	1.28 (1.22)	1.32 (1.25)
	Oct-III	Zn	1.36	1.33 (1.25)	1.30 (1.25)	1.33 (1.26)
	Tet-I	Zn	1.37	1.24 (1.15)	1.31 (1.22)	1.33 (1.28)
O-B vacancy	*Oct-I*	Sn	2.52	1.77 (2.06)	2.10 (2.14)	2.52 (2.26)
	Oct-II	Zn	1.36	1.30 (1.29)	1.30 (1.27)	1.38 (1.26)
	Oct-III	Sn	2.52	2.11 (2.16)	2.29 (2.20)	2.55 (2.28)
	Tet-I	Zn	1.36	1.26 (1.19)	1.30 (1.24)	1.38 (1.27)

[a]Values in parentheses correspond to those without atomic relaxation.

Figure captions

Fig. 1. (a) Atomic structure of the perfect ZTO supercell and (b) magnified viewing around *O-A* and *O-B vacancies*, respectively. Blue, orange and black circles indicate Zn, Sn and O atoms.

Fig. 2. Image charge corrections of the formation energies according to the various methods for (a) V_O^+ and (b) V_O^{2+} at the *O-A site* using PBE+U.

Fig. 3. Formation energies of V_Os for *O-A* and *O-B* vacancies in ZTO as a function of Fermi level at the O-rich condition using opt-HSE06 with the LZ correction..

Fig. 4. Band structures of (a) perfect ZTO, ZTO with V_O^0 for the (b) unrelaxed, (c) relaxed atomic configuration, and ZTO with V_O^{2+} for the (d) unrelaxed, (e) relaxed atomic configuration in the case of the *O-A vacancy*. Occupied and unoccupied bands are described as solid lines and dashed lines, respectively. (f) PDOSs of Sn at *oct-I* and Zn at *oct-II* sites, which are located at the two nearest octahedral sites from the V_O^0. PDOSs for the perfect ZTO are also shown for comparison. The PDOS in CBM is thirty times magnified for better viewing. Shadow regions indicate the bandgap of pure ZTO. The energy is shifted to the VBM of pure ZTO.

Fig. 5. The $|\Psi|^2$ plots of the localized band occupied by two electrons induced by the V_O^0 for (a) *O-A* and (b) *O-B vacancy*. The a, b, c and d cations are the same as Fig. 1b. Isosurface level is 0.005 electrons/Å^3. Blue, orange circles indicate Zn, Sn atoms, respectively.

Fig. 6. Atomic configuration diagram for optical ionization energy from V_O^0 to ($V_O^+ + e^-$) and that from ($V_O^+ + e^-$) to ($V_O^{2+} + 2e^-$) for (a) *O-A* and (b) *O-B vacancy*. The E_F is located at the CBM.

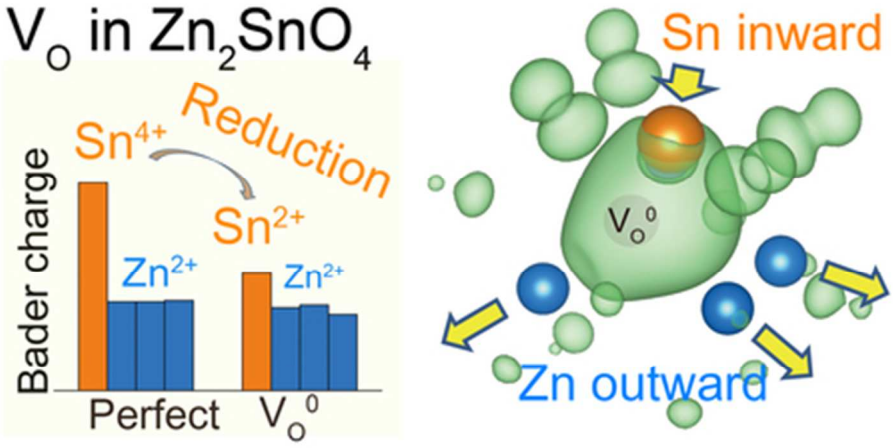

39x19mm (300 x 300 DPI)

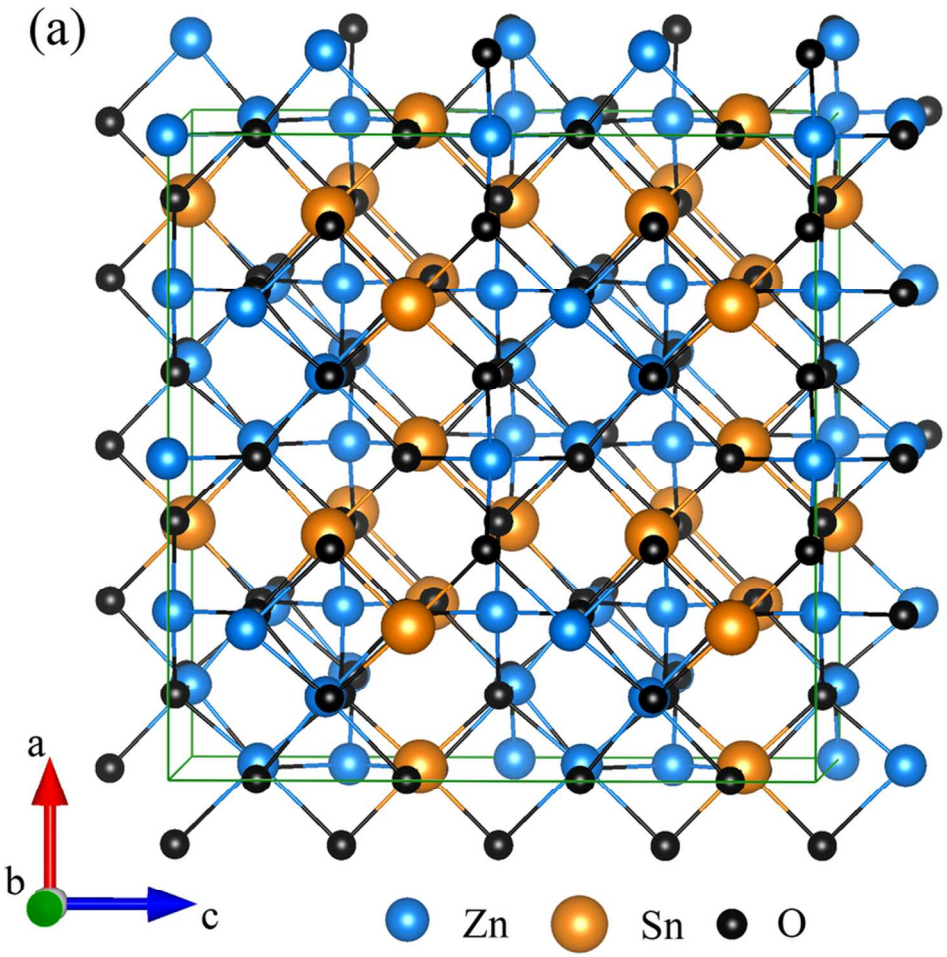

80x80mm (300 x 300 DPI)

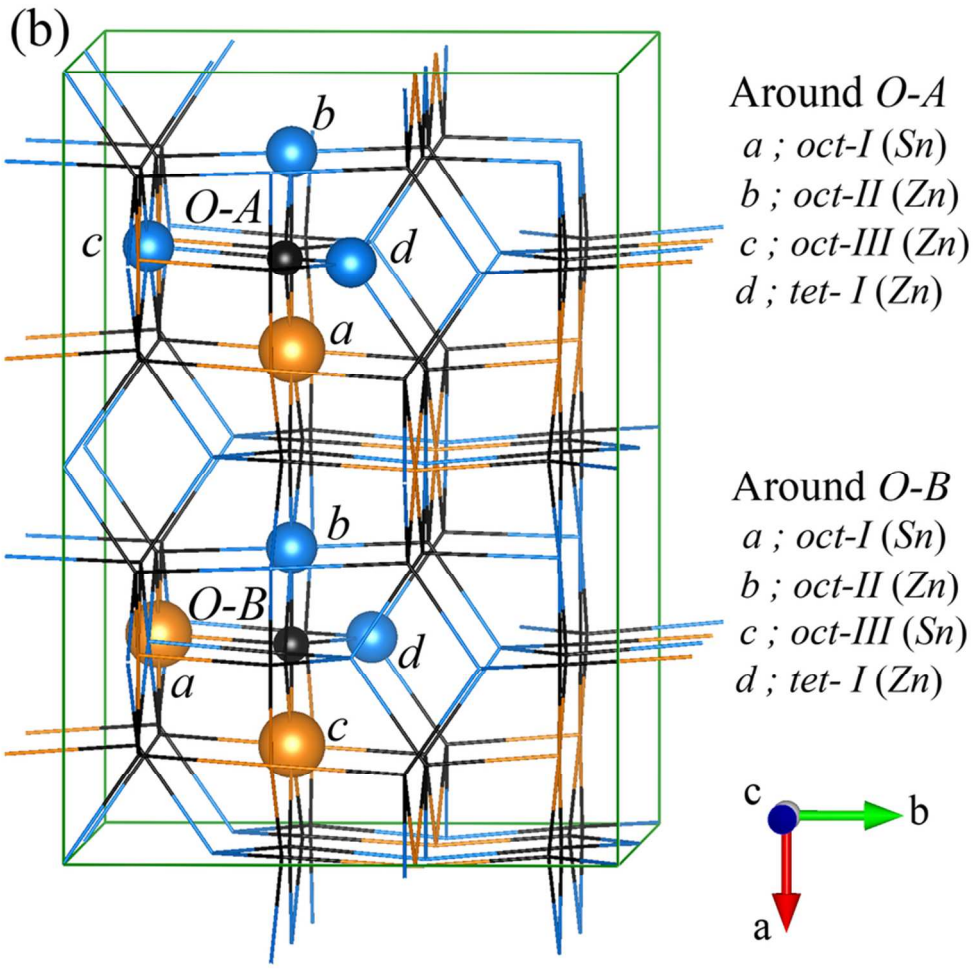

80x80mm (300 x 300 DPI)

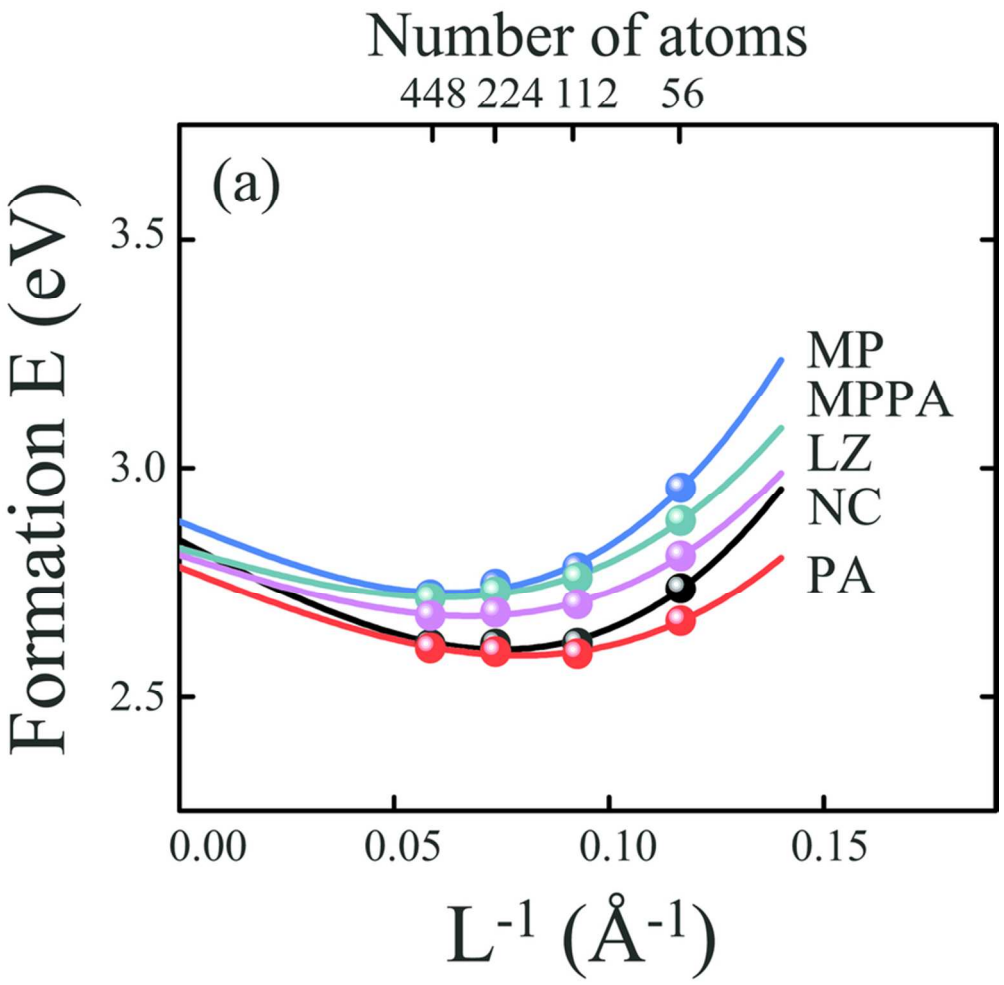

77x75mm (300 x 300 DPI)

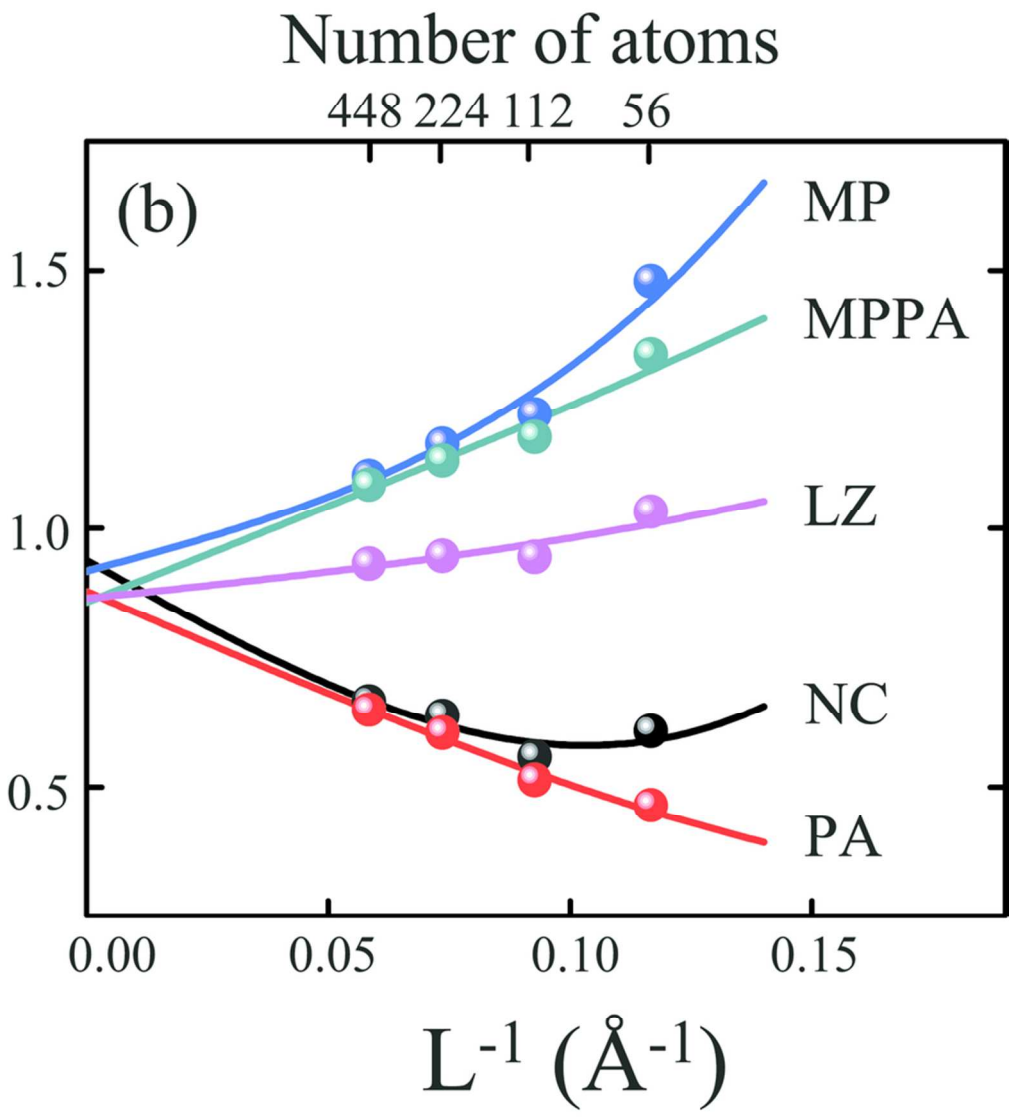

77x86mm (300 x 300 DPI)

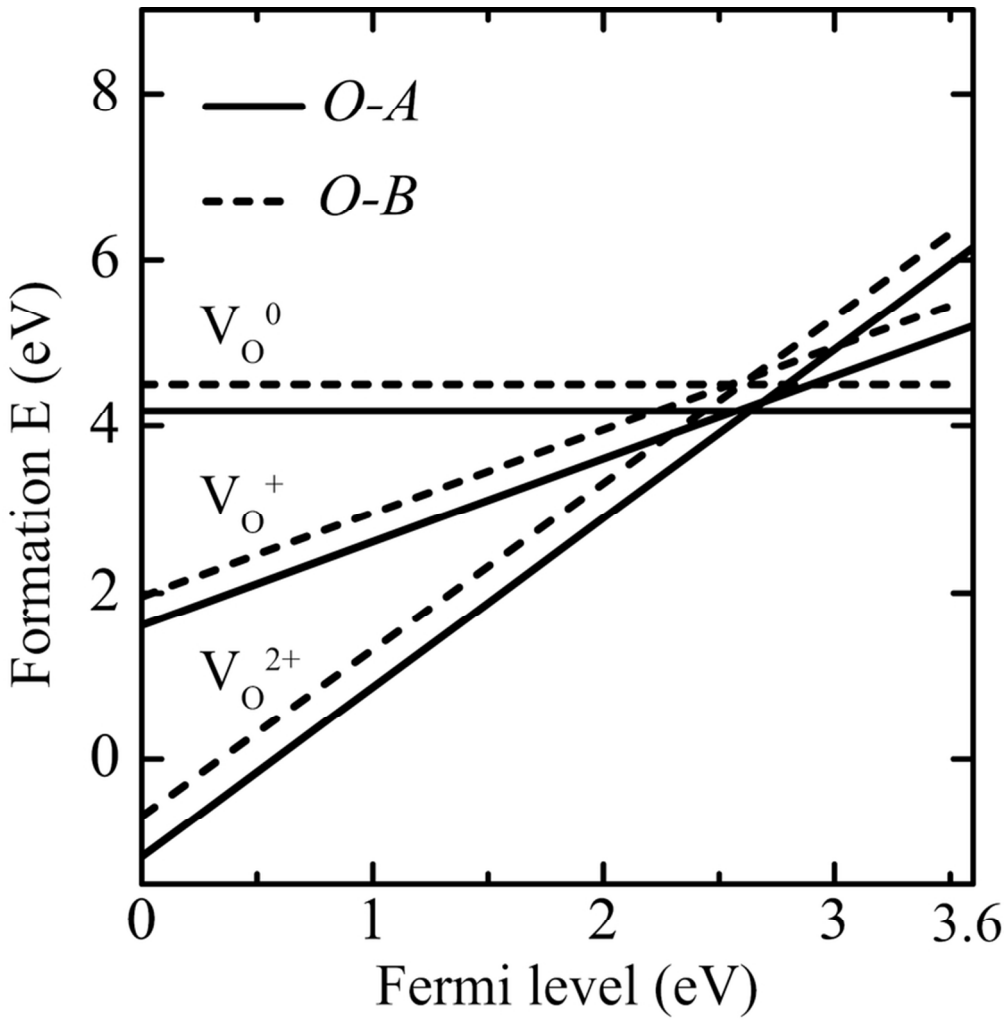

74x75mm (300 x 300 DPI)

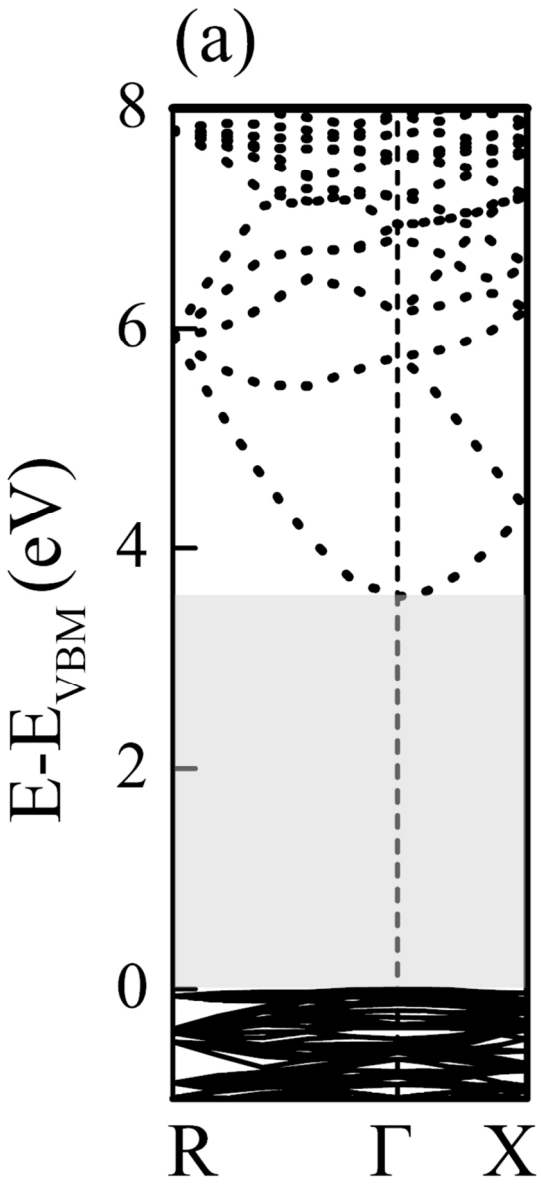

67x150mm (300 x 300 DPI)

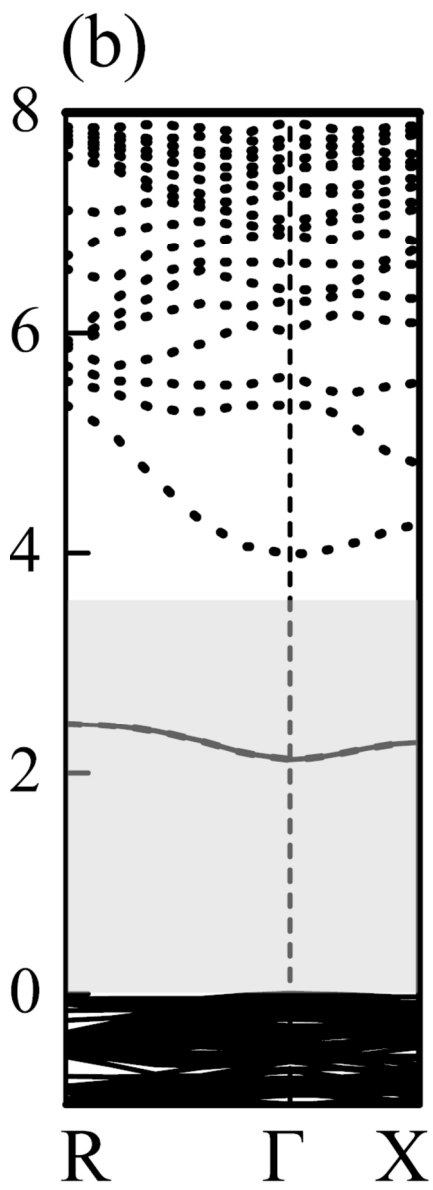

67x192mm (300 x 300 DPI)

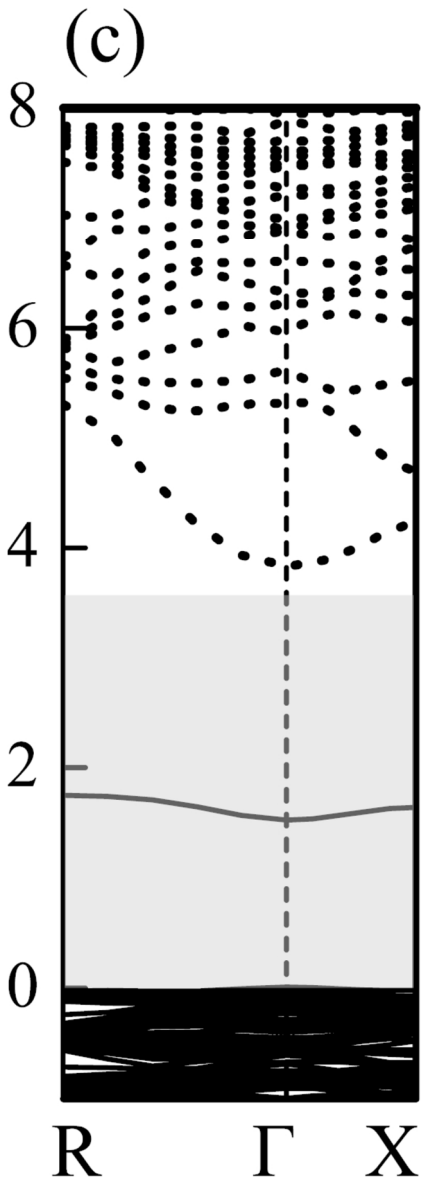

67x195mm (300 x 300 DPI)

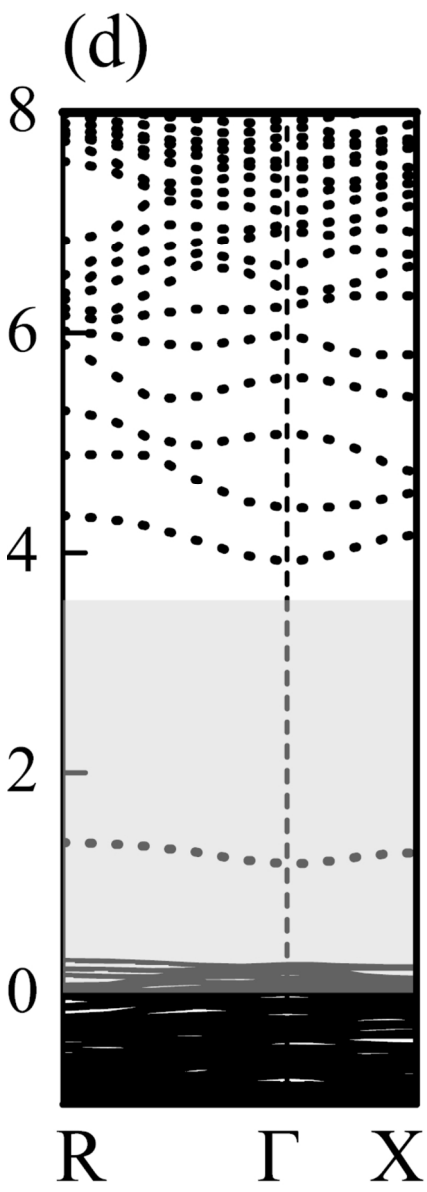

67x193mm (300 x 300 DPI)

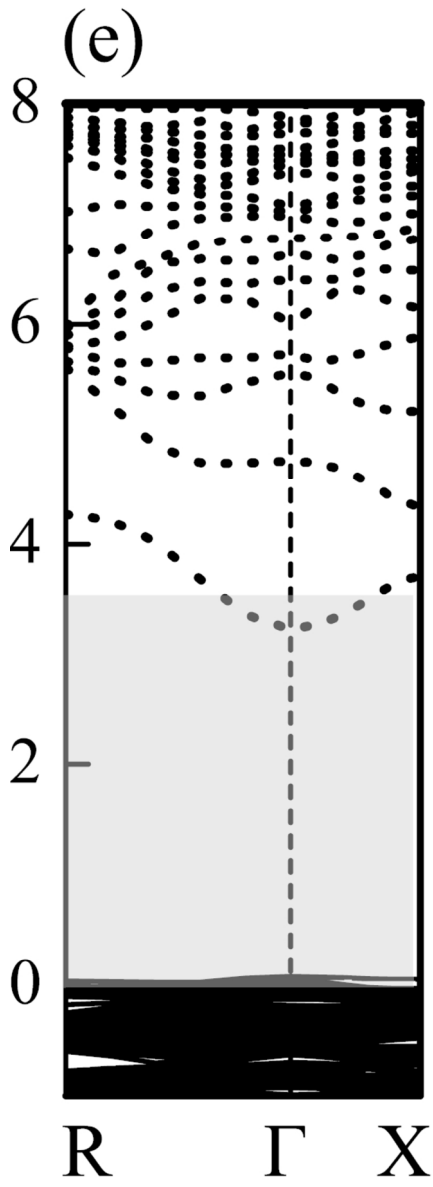

67x192mm (300 x 300 DPI)

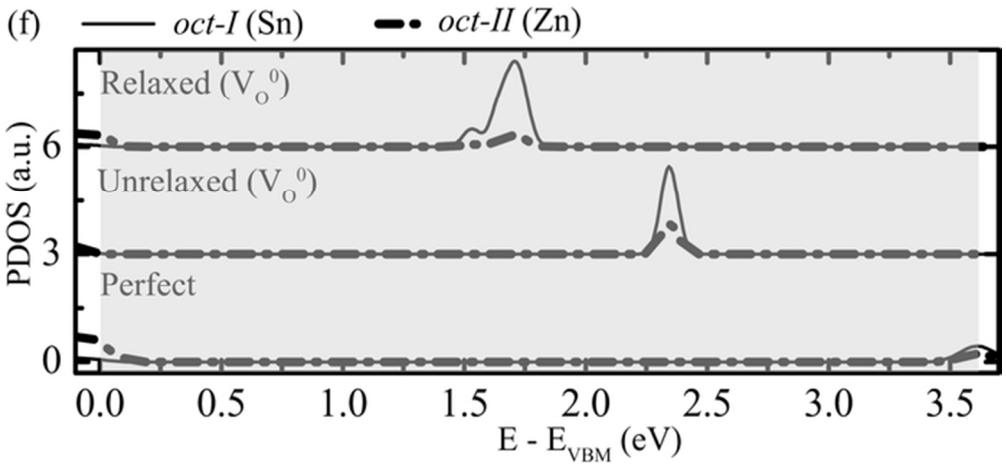

58x27mm (300 x 300 DPI)

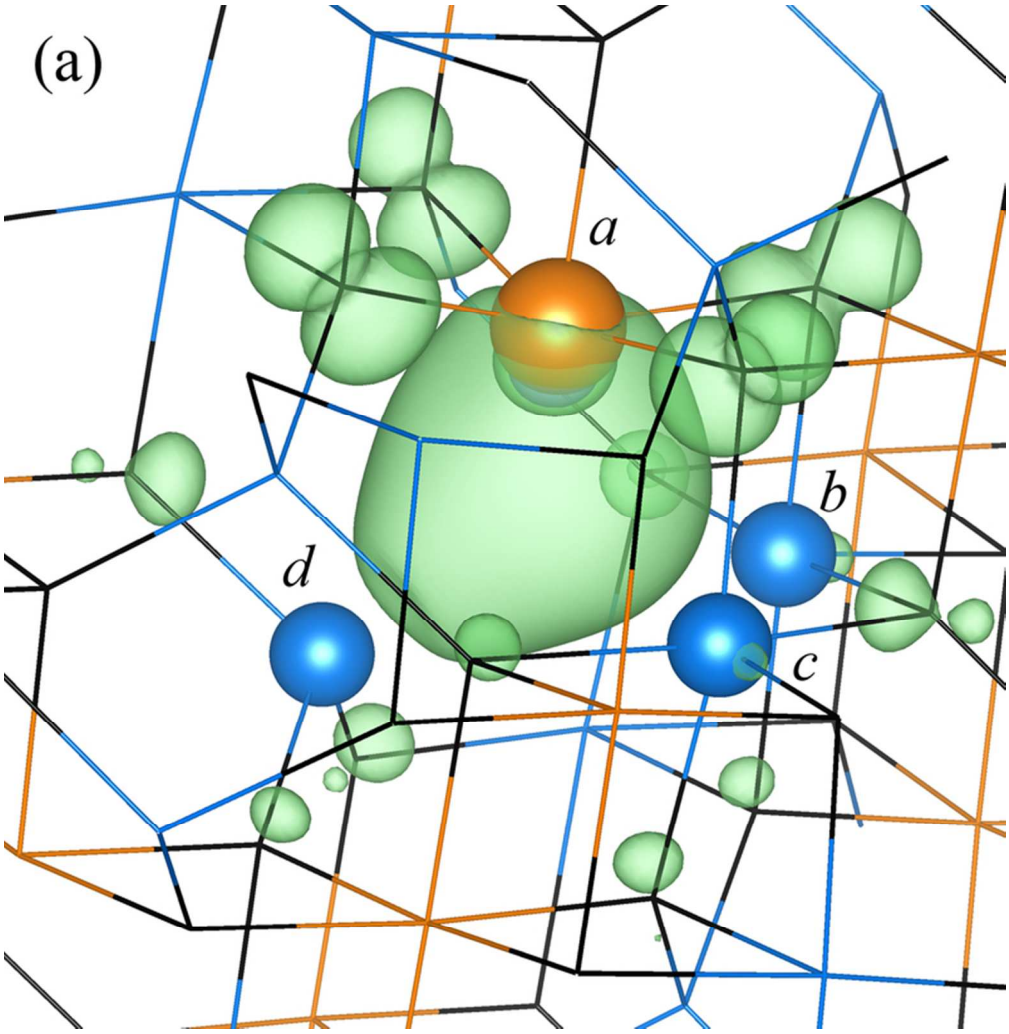

67x69mm (300 x 300 DPI)

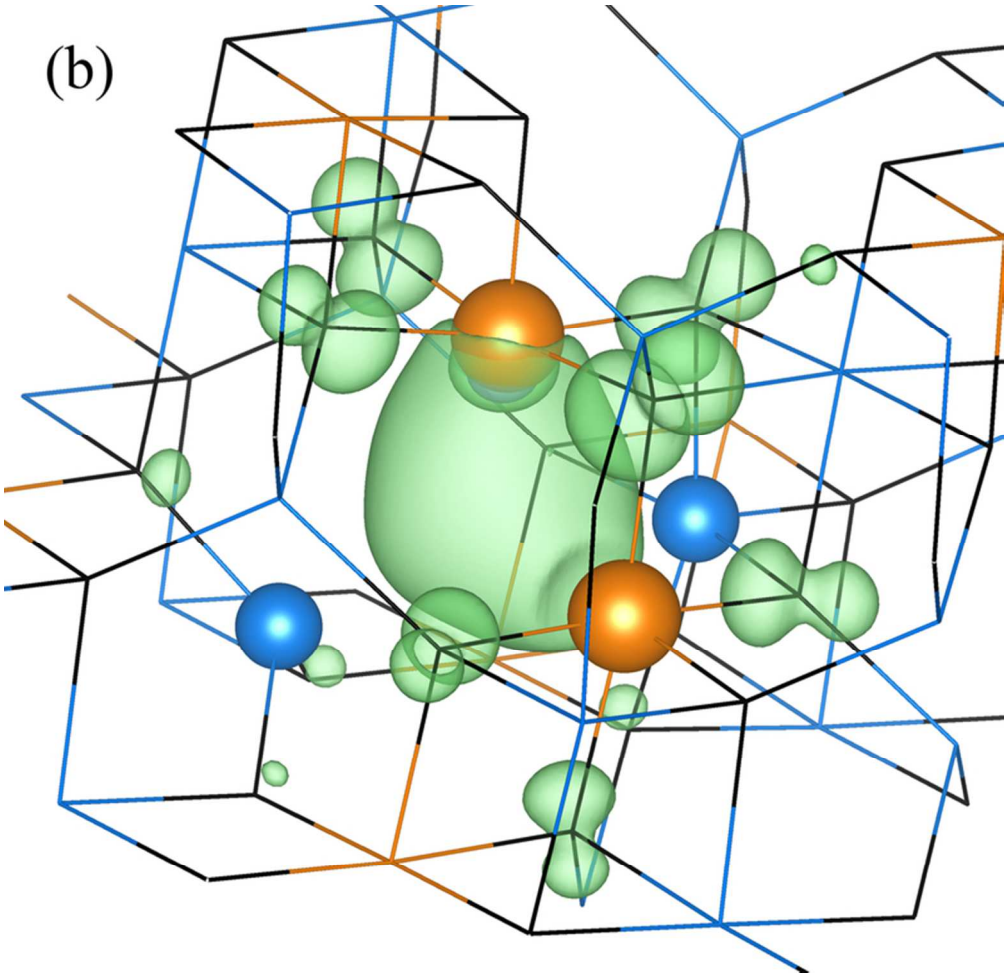

67x65mm (300 x 300 DPI)

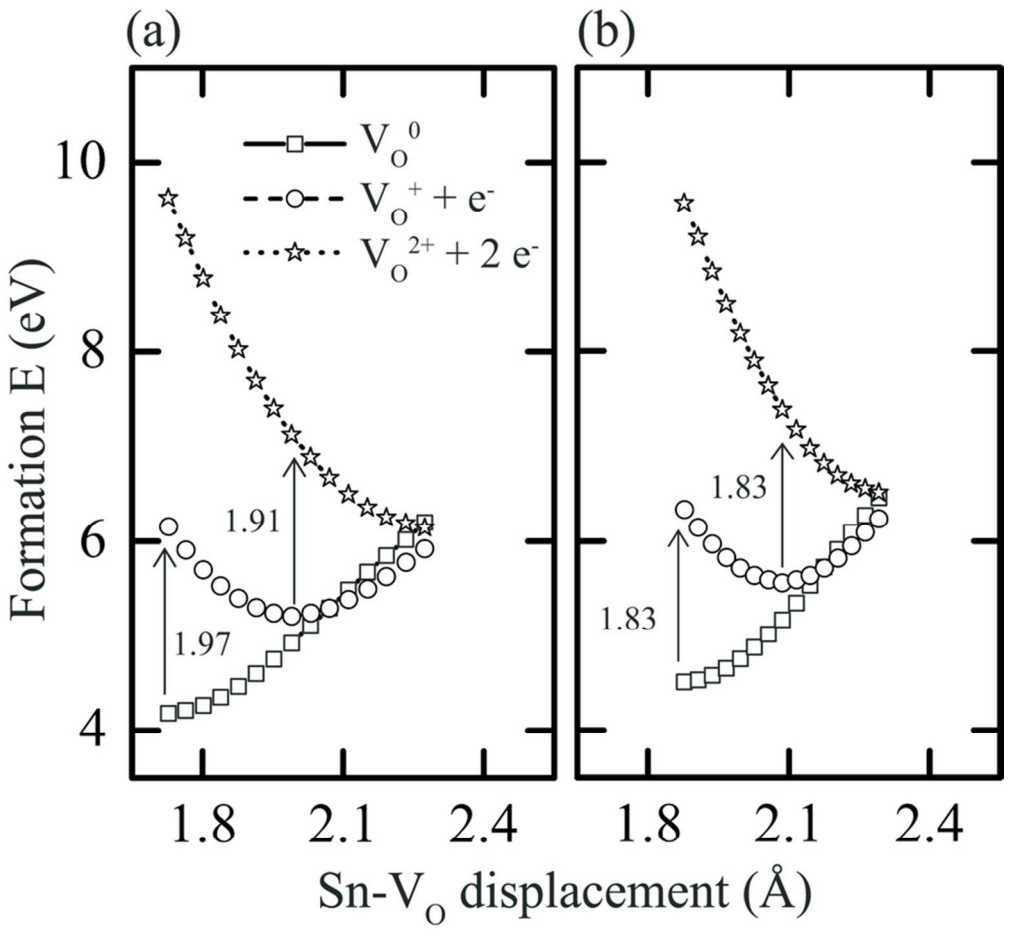

77x72mm (300 x 300 DPI)